Remodeling of lipid-foam prototissues by network-wide tension fluctuations induced by active particles

Andre A. Gu[1,2], Peter Tran[2], Arthur Prindle[2,3,4], Neha P. Kamat[1,3,5], Jan Steinkühler[1,6,7]*

[1] Department of Biomedical Engineering, Northwestern University, Evanston, IL, 60208, USA
[2] Department of Chemical and Biological Engineering, McCormick School of Engineering, Northwestern University, Evanston, IL, 60208, USA
[3] Center for Synthetic Biology, Northwestern University, Evanston, IL, 60208, USA
[4] Department of Biochemistry and Molecular Genetics, Feinberg School of Medicine, Northwestern University, Chicago, IL, 60611, USA
[5] Chemistry of Life Processes Institute, Northwestern University, Evanston, IL 60208, USA
[6] Bio-Inspired Computation, Kiel University, Kaiserstraße 2, 24143, Kiel, Germany
[7] Kiel Nano, Surface and Interface Science KiNSIS, Kiel University, Christian-Albrechts-Platz 4, 24118, Kiel, Germany

*corresponding author jst@tf.uni-kiel.de

Abstract
Recent advances in the field of bottom-up synthetic biology have led to the development of synthetic cells that mimic some features of real cells, such as division, protein synthesis or DNA replication. Larger assemblies of synthetic cells might be used to form proto-tissues. However, existing proto-tissues are limited by their relatively small lateral dimensions or lack of remodeling ability. In this study, we introduce a lipid-based tissue mimetic that can be easily prepared and functionalized, consisting of a millimeter-sized "lipid-foam" with individual micrometer-sized compartments bound by lipid bilayers. We characterize the structural and mechanical properties of the lipid-foam tissue-mimetic. We demonstrate self-healing capabilities enabled by the fluidly of the lipid bilayers. Upon inclusion of bacteria in the tissue compartments we observe the tissue-mimetic exhibits network-wide tension fluctuations driven by cooperative interactions of swimming bacteria. Active tension fluctuations facilitate fluidization and reorganization of the lipid foam tissue mimetic, providing a versatile platform for understanding and mimicking biological tissues.

Introduction
Recent developments have led to the development of synthetic cells that are able to mimic some features of real cells[1], such as membrane fusion,[2,3] division,[4,5] and DNA replication.[6] It would be highly desirable to transfer these advances to larger, tissue-like, scales. Conceptually, the construction of larger tissue mimetics demands engineering of adhesive interactions between individual synthetic cells. This is challenging because on one hand the interactions need to be strong enough for stabilization of tissue-scale structures, on the other hand they need to allow for dynamic reorganization,[7] a hallmark of biological tissues. For example, cross-linked population of giant unilamellar vesicles were shown to assemble to millimeter sized prototissues,[8] but these structures appear static after assembly, indicating they miss the fluidity of biological tissues. Impressive advances have been made by construction of proto-spheroids where shaped changes could be fueled by enzymatic reactions, but spheroids were sized only about 100 µm, indicating too weak stabilizing interactions for the formation of larger tissue mimetics. Importantly, printed lipid monolayer coated droplets immersed in an oil phase (droplet interface bilayers, DIBs) have been also

suggested as a tissue mimetic[9–11], such droplet networks reach millimeter sizes and allow for osmotically-induced reshaping. However osmotically induced forces are typically much larger than forces generated by molecular motors, which should be sufficient to remodel bio-inspired tissues. Additionally, the surrounding oil phase limits the DIB biocompatibility for biological parts added from the outside and preparation by custom-made printers limits the readily adoption of these methods. Most recently DIB were transferred from the oil phase a water phase, but the resulting structures were either limited in their size or no remodeling abilities were demonstrated[12–14]. Taken together, there is still a lack of generally available water-immersed millimeter sized tissue mimetic that is compatible with the developments in the synthetic cell field and is able undergo dynamic remodeling events.

Here we introduce a lipid-based tissue mimetic that can be readily prepared and functionalized. The structural basis for our tissue mimetic is the assembly of a millimeter sized “lipid-foam” with individual micrometer-sized compartments. Biological tissues are often described as a type of active foam in physical models.[15] Throughout this work, we compare and point out the connection of foam-like properties between our tissue mimetic and biological tissues. We demonstrate the tissue-mimetic has self-healing capabilities enabled by dynamic reorganization of subcompartments and introduce active tissue fluctuations through encapsulation of bacteria that drive remodeling events and generate forces onto the environment.

This work is divided into three parts. First, we describe the assembly of a millimeter-scale lipid foam using a microfluidics and phase transfer method. Second, we characterize the resulting structure in terms of its assembly rules and mechanical properties. Third, we induce active tension fluctuations by swimming bacteria, which we show drives large-scale fluidization and reorganization of the lipid foam tissue mimetic.

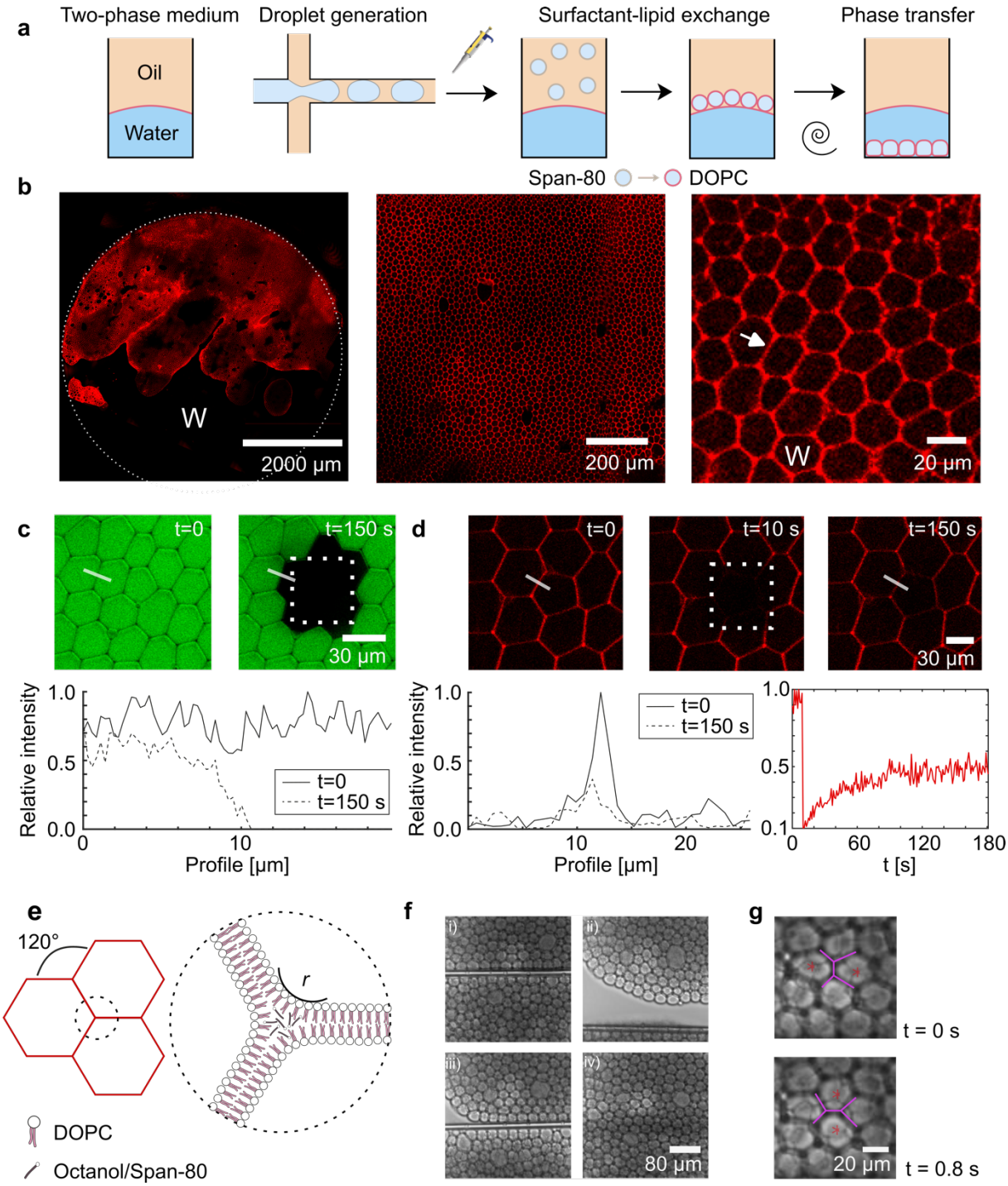

Figure 1. Characterization of lipid-based tissue mimetic. (a) Schematic for preparing tissue mimetic structures. (b) Biomimetic structure consists of 20 µm in diameter compartments spanning many millimeters in lateral size. Three examples at different location and magnification are shown. Red shows lipid analog fluorescence. Arrow highlights compartment boundaries as discussed in the main text. The letter W indicates the water phase (c) FRAP experiment performed on compartments encapsulated with water-soluble dye (green). Fluorescence did not recover over the experimental timescale, indicating that the dye cannot pass between compartments. Plot shows fluorescence intensity along the path of the white line. (d) FRAP experiment performed on lipid dye channel (red). A fraction of the fluorescence is not recovered, indicating that only one monolayer of the lipid bilayer is connected to neighboring compartments (left). Fluorescence recovery over time is shown (right). (e) Schematic of lipid junctions between compartments, *r* is the contact curvature radius below optical resolution (f) Series of events showing remodeling after mechanical loading: i) Scission by mechanical loading ii) Induction of a defect by movement of the pipette iii) compartments are brought back into contact iv) removal of pipette and "healing" of the structure (g) enlarged view of a T1 transition observed during step iv.

Results

Our initial goal was to create a suitable structural scaffold for our tissue mimetic. We achieved this by combining and adapting existing methods of flow-focusing microfluidic droplet formation,[16] droplet interface bilayers (DIB),[17–19] and emulation phase transfer.[20,21] On a microfluidic chip, we prepared 20 - 50 µm water-in-oil emulsion droplets stabilized with the surfactant Span 80 (Fig. 1a). Microfluidic droplets were generated, and a concentrated droplet emulsion was transferred into mineral oil that contained the phospholipid 18:1 (Δ9-Cis) PC (DOPC). Volumes were chosen such that DOPC was in excess concentration to SPAN 80 and equilibrated to exchange most Span 80 on the droplet surface with a self-assembled monolayer of DOPC molecules. The mineral oil comprised the top layer of a two-phase liquid system with a water layer at the bottom (Fig 1a). The resulting droplet concentration in the oil phase was chosen such that approximately a single layer of droplets sedimented at the oil-water interface. Droplets were then transferred into the water phase via centrifugation. The result was a structure consisting of 20 - 50 µm large aqueous compartments, which were immersed in an outer water phase and overall spanned many millimeters in lateral size (Fig. 1b). We found that the here established sequence of assembly steps was important, as it allows the stabilization of single homogenously sized single droplets in the microfluidic chip and triggers assembly into a droplet network by exchange of surfactant for lipid only before the structure is finally transferred into an outer water phase. The structures assembled in the established conditions were remarkably stable and lasted days without obvious degradation in overall morphology.

We next characterized the structural properties of the tissue mimetic. The obtained structure is approximately two-dimensional – its lateral size is on the scale of millimeters and its height is in the range of 20 - 100 µm. However, the structure was not always a single monolayer, as we often observed two or more layers of compartments stacked on top of each other. The optical density of the compartments did not allow us to study these stacked elements in detail, so we focused on the bottom hexagonal packed honeycomb lattice (Fig. 1b). Fluorescent images showed straight lamellae between individual compartments (arrow in Fig. 1b). The fluorescent dye used to visualize the compartments is a lipid analog. To confirm the lipids assembled into bilayers between compartments, we introduced the protein α-hemolysin (αHL) into the surrounding water phase. In lipid bilayers, but not thicker emulsion shells, αHL monomers assemble into membrane pores.[22,23] We monitored the permeability of the compartment boundaries using a membrane-impermeable dye. Only in the presence of αHL did the dye intensity decrease over time (Fig. S1), confirming that the compartments are separated by lipid bilayers with a thickness of 3 - 5 nm. Another feature that is visible in the microscopic images is that bilayer segments often intersect to form three-way junctions (Fig. 1b). We refer to these junctions as vertices. To characterize the nature of the contact between lipid bilayers and vertices, we performed fluorescent bleaching experiments (FRAP). Bleaching a rectangular section of encapsulated water-soluble dye (as shown in Fig. 1c), we observed that the bilayers were intact and impermeable to water-soluble molecules as expected. FRAP of the lipid analog dye resulted in the recovery of fluorescence within minutes, demonstrating the lipid bilayers are fluid (Fig. 1d). Interestingly, only up to half of the original fluorescence was recovered, indicating that only one monolayer of the lipid bilayer had recovered its fluorescence. This incomplete recovery suggested that lipid transfer between compartments was not possible and that a single continuous monolayer enclosed each compartment. While lipids are confided to the individual compartments, smaller, hydrophobic molecules (e.g. residual oil from the phase transfer procedure) might diffuse in the continuous bilayer/vertex

phase (Fig S2). From these experiments and geometric considerations, we concluded that the microscopic configuration of a vertex consists of three lipid bilayers unzipping at a vertex with a small (sub-diffraction) volume in the center and with a radius of curvature *r* between the lipid bilayer thickness and the optical resolution limit of about 500 nm (Fig. 1e).

From the deduced structure some quantitative estimates can be made. From experiments on black lipid membranes, it is known that the surface tensions of the vertex monolayers γ_{ML} balance the tension in the lipid bilayer γ_B with a microscopic contact angle ϕ.[24]

$$(1)\ \gamma_B = 2\gamma_{ML}\cos(\phi)$$

Typical values for lipid/surfactant monolayer to water interfacial tension γ_{ML} are on the order of 1 mN/m. We do not know the exact value of the microscopic contact angle ϕ, but in similar systems a value of $\phi \approx 52°$ has been found, which would result in a bilayer tension γ_B of about 1.2 mN/m.[25,26] These values are comparable to cortical tensions measured in tissues or isolated plasma membranes. It is important to note that the microscopic contact angle should be distinguished from the angle at which the bilayers meet at a vertex – the angle at which the lipid bilayers meet is always close to 120° consistent with a force balance between the three bilayers (Fig 1e). Together with the approximately equal compartment volumes, due to their microfluidic preparation, the bilayer tensions lead to the formation of an ordered lattice analogous to Plateau's laws in foams.[24] It is also interesting to considerer that the vertices correspond to collapsed Plateau border in dry foams. This analogy and variational energy calculations suggest that the vertices contribute a stabilizing role for the tissue mimetic, in other words, they have a negative line tension on the order of $\gamma_B r$.[27] Unlike in foams, however, the compartments are filled with water rather than air, and the compartments are divided by lipid bilayers and not water films, making the structure a better mimetic of biological tissues. This analysis highlights three crucial components of our tissue mimetic: Membrane fluidity, stabilizing forces by interplay of geometry to lipid self-assembly, and biocompatibility.

An essential feature of biological tissues is their ability to remodel. Tissue remodeling and fluidization of biological tissue is enabled by exchange of neighboring cells by so-called T1 transitions.[28] A T1 transition is a topological rearrangement event, where one cell edge shrinks to a point and then expands in a perpendicular direction, resulting in the swap of neighboring cells. We observed a similar remodeling upon mechanically loading our structure (Movie M1, Fig. 1f i). When we divided neighboring compartments by moving a micropipette into the plane of the structure, we found that the compartments stayed intact. We observed that the structure reacted to the mechanical loading and within seconds to minutes the compartments reorganized to minimize their surface energy (Fig 1f ii). When brought back into contact, the split structure resealed in a self-healing manner (Fig 1f iii – iv). In this process, we observed that individual compartments could pass each other, resulting in compartments exchanging positions by a T1 transition (Fig 1g). We interpret this series of events as loading above the yielding stress, which was sufficient to fluidize the otherwise jammed, close packed, structure. The physical basis for the remodeling ability is the fluidity of lipid membranes and the ability of two monolayers to slide relative to each other in a process called intermonolayer slip. Values for the intermonolayer slip range from 10^6–10^7 dyn s cm^{-3},[29] and should be indicative for the viscosity of the composite structure. These results showed that we can mimic the ability of biological tissues to react to external mechanical loading by inducing dynamic reorganization.

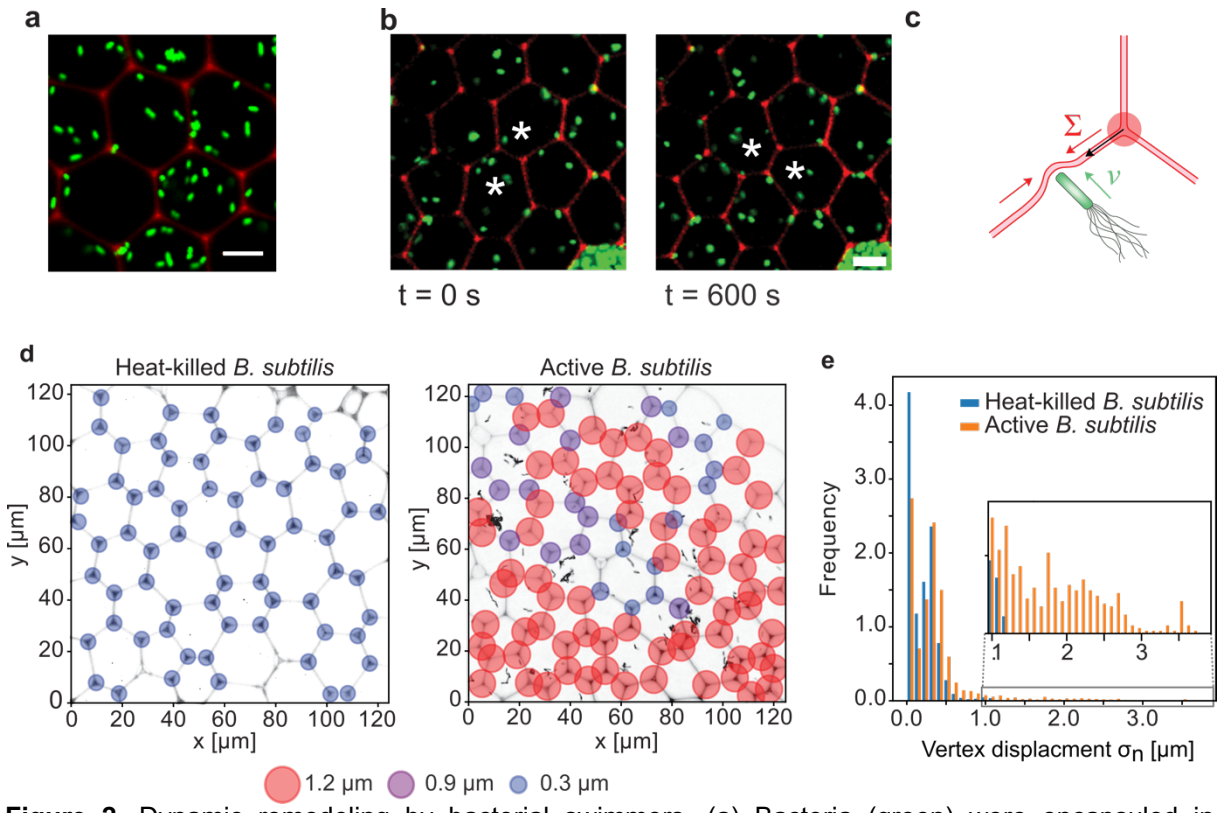

Figure 2. Dynamic remodeling by bacterial swimmers. (a) Bacteria (green) were encapsuled in compartments (lipid dye in red). (b) Spontaneous T1 transition observed with encapsuled bacteria. Stars indicate two neighboring compartments before (t = 0 s) and after (t = 600 s) the remodeling event. (c) Schematic shows how vertex displacement relates to membrane tension generation by collision of bacteria with lipid bilayer. (d) Spatial mapping of measured vertex displacement. Size and color of circles indicates the amplitude of the largest observed displacement over a timeframe of 10 minutes. (e) Histogram of vertex displacement obtained for active and heat-killed bacteria. Inset shows enlarged view of the indicated region. All scale bars are 10 μm.

So far, we have characterized the lipid foam scaffold in its equilibrium properties and passive response to external mechanical loading. Yet, cells also exert forces on their environment, resulting in dynamic changes of tissue stresses, which ultimately drive tissue reorganization. In previous studies, membrane tension has been induced by collisions between active particles, such as chemically fueled swimmers or bacteria, and lipid bilayers[30,31]. Therefore, we hypothesized that by encapsulating bacteria into the compartments, we could induce active stresses in the tissue-like scaffold. We found that our encapsulation procedure successfully produces compartments with live, swimming *B. subtilis* bacteria (Fig 2a, Movie M2). We found that in the order of 10 to 100 bacteria were encapsuled per compartment. Visual inspection showed that the swimming bacteria collided with the bilayer membranes, transferring energy between the bacteria and membranes. Swimming speeds of live bacteria are on the order of 20 μm/s, meaning that within the 20 - 50 μm diameter compartments, many collisions occur on the timescale of minutes. We reasoned that over longer timescales the stresses induced by the bacteria might induce remodeling events and consequently observed our hybrid synthetic-bacterial structure over many hours. Strikingly, the generated stresses seemed to drive T1 transitions from within the tissue (Fig 2b). To determine whether the magnitude of stresses generated are sufficient to drive this dynamic reorganization, we obtained detailed statistics of individual vertex positions. The rationale for tracking vertex position is that it is dependent on the force balance between the three bilayer tensions; if unequal tensions between the three bilayers were developed, the vertex would be displaced from its equilibrium

position (Fig 2c). With this assumption, the displacement of vertices from their average positions was chosen to be a measure of the tissue mimetic tensions. We found that vertices of compartments filled with live bacteria showed larger displacements then heat-killed, non-swimming, bacteria (Fig. 2d). Averaging 600 frames and 68 vertex locations over 10 minutes, we found an average standard deviation in vertex position of 0.2 μm when heat-killed, passive, bacteria were encapsuled. The average standard deviation in vertex position was found to be 0.37 μm when live, swimming bacteria were encapsulated, a significant increase compared to that of heat-killed bacteria (Fig. 2e). Notably, the distribution of average displacements was not Gaussian; instead, a long tail of displacement values up to 3.5 μm were found with swimming bacteria (inset Fig. 2d). These large and rare displacements, spanning many microns, fell in the range of vertex distances, and were thus sufficient to drive T1 transitions.[15] Taking the determined membrane tension $\gamma_B = 1.2$ mN/m a displacement of 3.5 μm implies a force of about 8 pN, which is comparable to the force generated by membrane anchored molecular motors and sufficient to induce synthetic cell division[4,32]. These results demonstrate that bacterial swimmers can drive remodeling of the tissue mimetic by generation of membrane tension realistic for biological tissues.

We aimed to better understand the mechanism by which rare and large vertex displacements occur. Here, we considered the effect of the elastic lattice in which the bacteria confined. Both annihilation and cooperative force generation might be possible as vertices are coupled by the elastic response of the lipid bilayers (Fig. 3a). To systemically measure the effect of cooperative events, we measured the temporal cross-correlation between vertex displacements. A cross-correlation between the displacement of an individual vertex and every other vertex revealed a positive correlation in vertex motion up to a distance l_{corr} of about 50 μm (Fig 3b). This suggests that bacteria from neighboring compartments indeed generate tensions cooperatively. As each compartment has six neighbors, cooperative events might generate quite significant “hotspots” of excitations as shown in Fig. 3c. Here, an initially relaxed configuration undergoes a transient state with collective motion of many vertices which then relaxes back over a timescale of minutes. Taken together, we show that the elastic lattice allows for cooperative interaction between the swimmers that generate sufficiently large driving forces to induce tissue-like remodeling events.

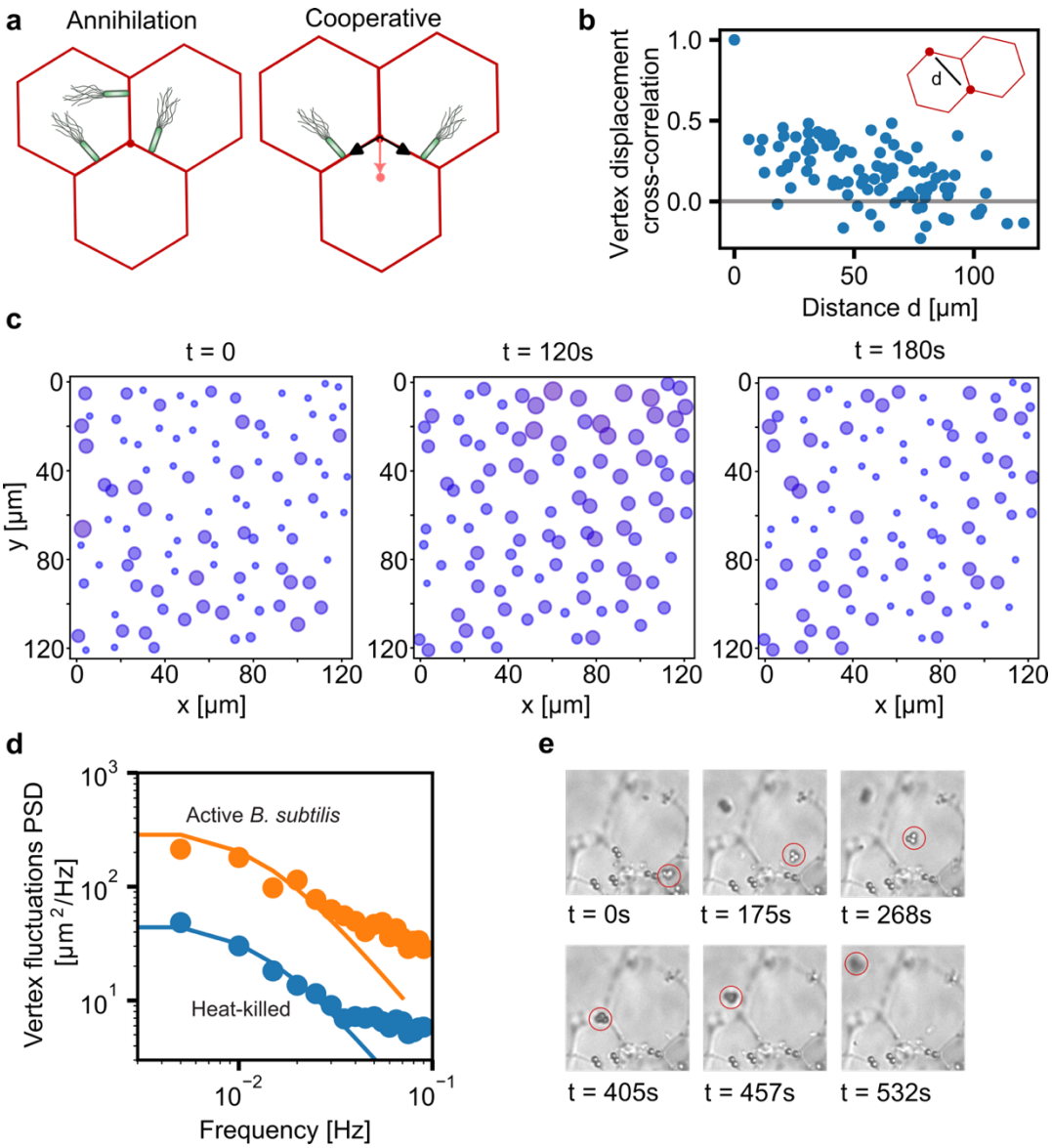

Figure 3. Coupling of bacterial swimmers in an elastic lattice. (a) Examples of possible interactions between bacterial swimmers in an elastic lattice. Left: Annihilation by interaction of three bacterial swimmers. Right: cooperative displacement of a vertex by two swimmers (b) Cross-correlation between two vertices separated by distance *d* over the displacement time series (c) Time series of maximum vertex displacement within 60-second segments. Sizes of circles are directly proportional to displacement magnitude. (d) Vertex fluctuations power spectral density (data points) and fit to Eq. (2) with parameters b = 0.5 μNs/m, $f_0 = 0.9 \times 10^{-3}$ Hz and T_{eff} = 6.5. (e) Time series showing two consecutive events of induced polystyrene bead movement (red circles).

To further expand our quantitative understanding of the chemical-mechanical coupling between swimming bacteria and deformations in the tissue mimetic, we consider a simplified one-dimensional lattice mode with elastic coupling between *N* vertices with displacement u_j. As the measured l_{corr} indicates that only nearest neighbors contribute to the coupling, we calculated the power spectrum of the Fourier transform $\mathcal{F}(u_0)$ for *N* = 2 (see Methods), which we then compare to the experimentally obtained power spectra.

(2) $|\mathcal{F}(u_0)|^2 = \frac{2k_bT_{eff}}{b(f^2+2f_0^2)}$

With the cross-over frequency $f_0 = \frac{k}{b}$, stiffness of the elastic coupling k, drag coefficient b, and (effective) temperature T_{eff}. Introduction of an effective temperature allows us to capture the

effect of the bacteria collisions, which, on sufficiently long timescales, appear as a random (uniformly distributed) force, a standard approach for systems with active particles. In the experiment, both alive and heat-killed bacteria groups showed a comparable spectrum to Eq. (2). Consistent with the previous analysis live bacteria show higher PSD values, corresponding to larger vertex displacement, than the head-killed control. For both samples some deviations towards higher frequencies were observed (Fit parameters are in caption of Fig. 3). The high-frequency deviations might stem from noise of the vertex detection which leads to leveling off for small sub-nanometer displacements. Additionally, at higher frequencies, deviations are expected as the effective temperature approximation is not valid anymore. Nevertheless, the approximate agreement between Eq. (2) and experiments allowed us to establish that: (1) The vertices indeed form an elastic lattice with coupling provided by the lipid bilayers, corroborating the model for cooperative tension generation suggested above, (2) The dynamics of the tissue mimetic were relatively slow with $f_0 \sim 10^{-2}$ Hz , with a large drag coefficient $b \sim 0.5$ μNs/m. These values were comparable to relaxation timescales found in in-vivo tissue measurements in the order of $10^{-1} - 10^{-2}$ Hz (Ref.[33]) and (3) The increase in effective temperature of $\frac{T_{eff}}{T} = 6.5$ by the encapsulated bacteria is comparable in magnitude found in biological systems. For example, ATP-driven membrane fluctuations in red blood cells result in $\frac{T_{eff}}{T} = 3$,[34,35] underlining the fact that the high densities of bacteria encapsulated here provide a strong non-equilibrium driving force. Taken together, these results demonstrate the tissue mimetic can be described as an elastic lattice that shows similar dynamics as biological tissues.

Finally, we showed that apart from driving internal reorganization, the active motion of vertexes was also dissipated to the environment. To demonstrate this, we attached microplastic beads to the surface of the biomimetic tissue (Fig. 3c, Movie M3). Only tissues with active motion of bacteria induced motion of the beads. If the beads were sufficiently close to the tissue edge, they were pushed off into the solution, demonstrating a simple “self-cleaning” effect driven by the bacterial motion. These experiments demonstrate that bacteria transduce chemical energy, from the nutrition they consume, into mechanical motion in the tissue mimetic structure through their swimming motion and elastic coupling.

Conclusion

In this work we have introduced a novel tissue mimetic based on a biocompatible lipid foam scaffold. We balance the contradicting requirements of a tissue mimetic by preserving membrane fluidity and strong stabilizing forces that emerge from the interplay of geometry and lipid self-assembly. By analogy between foams and tissues we have also described remodeling and self-cleaning abilities. Our results demonstrate how the individual motion of bacteria can be used to induce coordinated motion in structures that are about two orders of magnitude larger than individual bacteria. In the future, better spatial control of the active swimmers would be desirable. Here, swimmers that are sensitive to optical or electrical fields provide ways to locally induce stresses that would allow to control and steer remodeling events in synthetic tissue.

Methods

Materials

1,2-dioleoyl-sn-glycero-3-phosphocholine (DOPC) and 1,2-dioleoyl-sn-glycero-3-phosphoethanolamine-N-(lissamine rhodamine B sulfonyl) (ammonium salt) (Liss Rhod PE) were purchased from Avanti Polar Lipids. D-glucose, D-sucrose, mineral oil, Span-80

surfactant, phosphate-buffered saline (PBS) tablets, and polystyrene fluorescent beads (nominal diameter 2 μm) were obtained from Sigma-Aldrich. MSgg growth medium contains 5 mM potassium phosphate buffer (pH 7.0), 100 mM MOPS buffer (pH 7.0, adjusted using NaOH), 2 mM $MgCl_2$, 700 μM $CaCl_2$, 50 μM $MnCl_2$, 100 μM $FeCl_3$, 1 μM $ZnCl_2$, 2 μM thiamine HCl, 0.5% (v/v) glucose and 0.5% (w/v) monosodium glutamate, and were prepared using stock solutions at the current time.

Lipid mixture preparation

Liss Rhod PE was added to DOPC in chloroform to make a 4.6 mM mixture. The lipid formulation was dried under a nitrogen stream to create a thin film on the bottom of a 20 mL scintillation vial. The lipid films were placed in a vacuum chamber for 2 hours. Then, the films were resuspended in mineral oil and sonicated for 30 minutes in an ultrasound bath at 23°C, creating a 19 mM DOPC in mineral oil mixture.

Droplet generation using microfluidics

Within a well of a glass-bottomed 96-well plate, a two-phase liquid mixture was created. This mixture consisted of 150 μL of DOPC in oil mixture in the top layer and 150 μL of aqueous sucrose (600 mM) in the bottom layer. Droplets (~20 μm in diameter) of aqueous glucose (600 mM) in 4% Span-80 in mineral oil were generated on a PDMS microfluidic chip (Darwin Microfluidics). Using syringe pumps (Harvard Apparatus), the glucose and 4% Span-80 in oil streams were flowed into the chip at 1 μL/min and 4 μL/min, respectively. Droplets were collected in a pipette tip for 90 seconds before being transferred to the oil phase of a loaded plate well.

Creating droplets encapsulating bacteria

For bacterial encapsulation, the aqueous sucrose in the plate well was replaced by 150 μL of PBS buffer (~300 mOsM). PrpsD10 *Bacillus subtilis* NCIB3610 strains and MSgg media were prepared as described previously. The *Bacillus subtilis* strain was grown in MSgg media for 16 hours at 37°C. Before encapsulation, the optical density (OD_{600}) was measured via UV-vis spectrophotometry (Agilent Cary 60), and the osmolarity was recorded with a vapor pressure osmometer (VAPRO). To prevent osmolarity and density imbalances that can destabilize the compartments, glucose was added to the bacteria culture to match the osmolarity of the PBS solution. The osmolarity-adjusted bacteria suspension was then encapsulated into droplets at OD_{600} between 1.3 and 1.6 as described above.

Network formation via double emulsion

After droplet generation and transfer into wells, surfactant-lipid exchange was allowed to occur for 15 minutes. The droplets were then centrifuged at 3200 g for 5 minutes at room temperature, forming double emulsions of compartments at the bottom of the plate well.

Fluctuation analysis

Compartments were imaged with confocal microscopy (Nikon Eclipse Ti) at 200x. Timelapses were captured at 1 image per second over 10 minutes. Using ImageJ (National Institutes of Health, Version 2.3.0), individual vertices were isolated and smoothed, creating timelapses of individual vertices. For each frame in the timelapse, the pixel with the greatest intensity was identified to represent the vertex's position.

Downstream analysis was conducted using Jupyter Notebook and NumPy (version 1.20.1). To measure fluctuations, timelapses for each vertex were divided into 1-minute blocks. The standard deviation of the vertex's positions over one time block was taken to represent the

amplitude of fluctuation. To create the fluctuation map, a standard deviation was found for each time block for an individual vertex. The maximum of these standard deviations was chosen to represent the characteristic amplitude of fluctuation for that vertex.

Depositing microplastic beads on compartment surface

After initial centrifugation, the top oil layer was removed and replaced with 1% aqueous microplastic bead solution. Then, the plate was centrifuged at 600 g for 10 minutes at room temperature to spin the beads down to the compartment surface. To capture bead movements over time, timelapses were captured at 1 image per second over 10 minutes using brightfield microscopy (Nikon Eclipse Ti).

Calculation of the power spectrum

The tension acting on vertex *j* is given by a force balance as $T_j = k(2u_j - u_{j+1} - u_{j-1})$, where u_j is the vertex displacement from its resting position and k is the stiffness of the elastic coupling between vertices. To study the dynamics of the system, we considered an overdamped Langevin equation where every vertex is subject to stochastic agitation by a diffusion term $\eta(t)$ with friction coefficient b. Consistent with the low Reynolds number in our experimental system, we balanced motion of the vertices with a damping coefficient *b* and the tension T_j, resulting in the equation $b\frac{du_j}{dt} = k(2u_j - u_{j+1} - u_{j-1})$, with a time constant $\tau = \frac{b}{k}$. To study the dynamics of the system, we considered an overdamped Langevin equation where every vertex is subject to stochastic agitation by a white noise diffusion term $\eta(t)$.

(3) $b\frac{du_j}{dt} = k(2u_j - u_{j+1} - u_{j-1}) + \eta(t)$

The power spectrum was calculated by taking the Fourier transform

(4) $-bi\omega t\, U_j(\omega) = k\left(2U_j(\omega) - U_{j+1}(\omega) - U_{j-1}(\omega)\right) + \Xi(\omega)$

For a lattice N=2 two linear equations with two unknows U_0 and U_1 are obtained. The resulting power spectrum $|U_0(\omega)|^2$ shown in eq. (2) was then calculated with $\Xi(\omega) * \bar{\Xi}(\omega) = k_B T$.

Supplementary Material

Supplementary Information with Figure S1.
Supplementary Movies M1 – M3.

Acknowledgments

This research was supported in part by the National Science Foundation under Grant No. 1844336 (NPK, JS) and MRSEC DMR-1720139 (AG). JS thanks Reinhard Lipowsky for discussions on stability of foams.

References

(1) Staufer, O.; De Lora, J. A.; Bailoni, E.; Bazrafshan, A.; Benk, A. S.; Jahnke, K.; Manzer, Z. A.; Otrin, L.; Díez Pérez, T.; Sharon, J.; Steinkühler, J.; Adamala, K. P.; Jacobson, B.; Dogterom, M.; Göpfrich, K.; Stefanovic, D.; Atlas, S. R.; Grunze, M.; Lakin, M. R.; Shreve, A. P.; Spatz, J. P.; López, G. P. Building a Community to Engineer Synthetic Cells and Organelles from the Bottom-Up. *eLife* **2021**, *10*, e73556. https://doi.org/10.7554/eLife.73556.

(2) Iorio, D. D.; Lu, Y.; Meulman, J.; Huskens, J. Recruitment of Receptors at Supported Lipid Bilayers Promoted by the Multivalent Binding of Ligand-Modified Unilamellar Vesicles. *Chem. Sci.* **2020**, *11* (12), 3307–3315. https://doi.org/10.1039/D0SC00518E.

(3) Chan, Y.-H. M.; van Lengerich, B.; Boxer, S. G. Effects of Linker Sequences on Vesicle Fusion Mediated by Lipid-Anchored DNA Oligonucleotides. *Proc. Natl. Acad. Sci.* **2009**, *106* (4), 979–984. https://doi.org/10.1073/pnas.0812356106.

(4) Steinkühler, J.; Knorr, R. L.; Zhao, Z.; Bhatia, T.; Bartelt, S. M.; Wegner, S.; Dimova, R.; Lipowsky, R. Controlled Division of Cell-Sized Vesicles by Low Densities of Membrane-Bound Proteins. *Nat. Commun.* **2020**, *11* (1), 905. https://doi.org/10.1038/s41467-020-14696-0.
(5) Dreher, Y.; Jahnke, K.; Schröter, M.; Göpfrich, K. Light-Triggered Cargo Loading and Division of DNA-Containing Giant Unilamellar Lipid Vesicles. *Nano Lett.* **2021**, *21* (14), 5952–5957. https://doi.org/10.1021/acs.nanolett.1c00822.
(6) van Nies, P.; Westerlaken, I.; Blanken, D.; Salas, M.; Mencía, M.; Danelon, C. Self-Replication of DNA by Its Encoded Proteins in Liposome-Based Synthetic Cells. *Nat. Commun.* **2018**, *9* (1), 1583. https://doi.org/10.1038/s41467-018-03926-1.
(7) Trappe, V.; Prasad, V.; Cipelletti, L.; Segre, P. N.; Weitz, D. A. Jamming Phase Diagram for Attractive Particles. *Nature* **2001**, *411* (6839), 772–775. https://doi.org/10.1038/35081021.
(8) Arulkumaran, N.; Singer, M.; Howorka, S.; Burns, J. R. Creating Complex Protocells and Prototissues Using Simple DNA Building Blocks. *Nat. Commun.* **2023**, *14* (1), 1314. https://doi.org/10.1038/s41467-023-36875-5.
(9) Cole, R. H.; Tang, S.-Y.; Siltanen, C. A.; Shahi, P.; Zhang, J. Q.; Poust, S.; Gartner, Z. J.; Abate, A. R. Printed Droplet Microfluidics for on Demand Dispensing of Picoliter Droplets and Cells. *Proc. Natl. Acad. Sci.* **2017**, *114* (33), 8728–8733. https://doi.org/10.1073/pnas.1704020114.
(10) Graham, A. D.; Olof, S. N.; Burke, M. J.; Armstrong, J. P. K.; Mikhailova, E. A.; Nicholson, J. G.; Box, S. J.; Szele, F. G.; Perriman, A. W.; Bayley, H. High-Resolution Patterned Cellular Constructs by Droplet-Based 3D Printing. *Sci. Rep.* **2017**, *7* (1), 7004. https://doi.org/10.1038/s41598-017-06358-x.
(11) Alcinesio, A.; Cazimoglu, I.; Kimmerly, G. R.; Restrepo Schild, V.; Krishna Kumar, R.; Bayley, H. Modular Synthetic Tissues from 3D-Printed Building Blocks. *Adv. Funct. Mater.* **2022**, *32* (7), 2107773. https://doi.org/10.1002/adfm.202107773.
(12) Elani, Y.; Law, R. V.; Ces, O. Vesicle-Based Artificial Cells as Chemical Microreactors with Spatially Segregated Reaction Pathways. *Nat. Commun.* **2014**, *5* (1), 5305. https://doi.org/10.1038/ncomms6305.
(13) Alcinesio, A.; Krishna Kumar, R.; Bayley, H. Functional Multivesicular Structures with Controlled Architecture from 3D-Printed Droplet Networks. *ChemSystemsChem* **2022**, *4* (1), e202100036. https://doi.org/10.1002/syst.202100036.
(14) Bolognesi, G.; Friddin, M. S.; Salehi-Reyhani, A.; Barlow, N. E.; Brooks, N. J.; Ces, O.; Elani, Y. Sculpting and Fusing Biomimetic Vesicle Networks Using Optical Tweezers. *Nat. Commun.* **2018**, *9* (1), 1882. https://doi.org/10.1038/s41467-018-04282-w.
(15) Kim, S.; Pochitaloff, M.; Stooke-Vaughan, G. A.; Campàs, O. Embryonic Tissues as Active Foams. *Nat. Phys.* **2021**, *17*, 859–866. https://doi.org/10.1038/s41567-021-01215-1.
(16) Hernández-Cid, D.; Pérez-González, V. H.; Gallo-Villanueva, R. C.; González-Valdez, J.; Mata-Gómez, M. A. Modeling Droplet Formation in Microfluidic Flow-Focusing Devices Using the Two-Phases Level Set Method. *Mater. Today Proc.* **2022**, *48*, 30–40. https://doi.org/10.1016/j.matpr.2020.09.417.
(17) Elani, Y.; Gee, A.; V. Law, R.; Ces, O. Engineering Multi-Compartment Vesicle Networks. *Chem. Sci.* **2013**, *4* (8), 3332–3338. https://doi.org/10.1039/C3SC51164B.
(18) Bayley, H.; Cronin, B.; Heron, A.; Holden, M. A.; Hwang, W.; Syeda, R.; Thompson, J.; Wallace, M. Droplet Interface Bilayers. *Mol. Biosyst.* **2008**, *4* (12), 1191–1208. https://doi.org/10.1039/b808893d.
(19) Huang, Y.; Fuller, G. G.; Chandran Suja, V. Physicochemical Characteristics of Droplet Interface Bilayers. *Adv. Colloid Interface Sci.* **2022**, *304*, 102666. https://doi.org/10.1016/j.cis.2022.102666.
(20) Pautot, S.; Frisken, B. J.; Weitz, D. A. Production of Unilamellar Vesicles Using an Inverted Emulsion. *Langmuir* **2003**, *19* (7), 2870–2879. https://doi.org/10.1021/la026100v.
(21) Moga, A.; Yandrapalli, N.; Dimova, R.; Robinson, T. Optimization of the Inverted Emulsion Method for High-Yield Production of Biomimetic Giant Unilamellar Vesicles. *Chembiochem Eur. J. Chem. Biol.* **2019**, *20* (20), 2674–2682. https://doi.org/10.1002/cbic.201900529.
(22) Chalmeau, J.; Monina, N.; Shin, J.; Vieu, C.; Noireaux, V. α-Hemolysin Pore Formation into a

Supported Phospholipid Bilayer Using Cell-Free Expression. *Biochim. Biophys. Acta BBA - Biomembr.* **2011**, *1808* (1), 271–278. https://doi.org/10.1016/j.bbamem.2010.07.027.
(23) Tilley, S. J.; Saibil, H. R. The Mechanism of Pore Formation by Bacterial Toxins. *Curr. Opin. Struct. Biol.* **2006**, *16* (2), 230–236. https://doi.org/10.1016/j.sbi.2006.03.008.
(24) Weaire, D. L.; Hutzler, S. *The Physics of Foams*; Clarendon Press, 1999.
(25) Venkatesan, G. A.; Lee, J.; Farimani, A. B.; Heiranian, M.; Collier, C. P.; Aluru, N. R.; Sarles, S. A. Adsorption Kinetics Dictate Monolayer Self-Assembly for Both Lipid-In and Lipid-Out Approaches to Droplet Interface Bilayer Formation. *Langmuir* **2015**, *31* (47), 12883–12893. https://doi.org/10.1021/acs.langmuir.5b02293.
(26) Beerlink, A.; Thutupalli, S.; Mell, M.; Bartels, M.; Cloetens, P.; Herminghaus, S.; Salditt, T. X-Ray Propagation Imaging of a Lipid Bilayer in Solution. *Soft Matter* **2012**, *8* (17), 4595–4601. https://doi.org/10.1039/C2SM00032F.
(27) Géminard, J.-C.; Żywocinski, A.; Caillier, F.; Oswald, P. Observation of Negative Line Tensions from Plateau Border Regions in Dry Foam Films. *Philos. Mag. Lett.* **2004**, *84* (3), 199–204. https://doi.org/10.1080/0950083010001646707.
(28) Duclut, C.; Paijmans, J.; Inamdar, M. M.; Modes, C. D.; Jülicher, F. Active T1 Transitions in Cellular Networks. *Eur. Phys. J. E* **2022**, *45* (3), 29. https://doi.org/10.1140/epje/s10189-022-00175-5.
(29) Merkel, R.; Sackmann, E.; Evans, E. Molecular Friction and Epitactic Coupling between Monolayers in Supported Bilayers. *J. Phys.* **1989**, *50* (12), 1535–1555. https://doi.org/10.1051/jphys:0198900500120153500.
(30) Takatori, S. C.; Sahu, A. Active Contact Forces Drive Nonequilibrium Fluctuations in Membrane Vesicles. *Phys. Rev. Lett.* **2020**, *124* (15), 158102. https://doi.org/10.1103/PhysRevLett.124.158102.
(31) Vutukuri, H. R.; Hoore, M.; Abaurrea-Velasco, C.; van Buren, L.; Dutto, A.; Auth, T.; Fedosov, D. A.; Gompper, G.; Vermant, J. Active Particles Induce Large Shape Deformations in Giant Lipid Vesicles. *Nature* **2020**, *586* (7827), 52–56. https://doi.org/10.1038/s41586-020-2730-x.
(32) Leduc, C.; Campàs, O.; Zeldovich, K. B.; Roux, A.; Jolimaitre, P.; Bourel-Bonnet, L.; Goud, B.; Joanny, J.-F.; Bassereau, P.; Prost, J. Cooperative Extraction of Membrane Nanotubes by Molecular Motors. *Proc. Natl. Acad. Sci.* **2004**, *101* (49), 17096–17101. https://doi.org/10.1073/pnas.0406598101.
(33) Bambardekar, K.; Clément, R.; Blanc, O.; Chardès, C.; Lenne, P.-F. Direct Laser Manipulation Reveals the Mechanics of Cell Contacts in Vivo. *Proc. Natl. Acad. Sci.* **2015**, *112* (5), 1416–1421. https://doi.org/10.1073/pnas.1418732112.
(34) Gov, N. S.; Safran, S. A. Red Blood Cell Membrane Fluctuations and Shape Controlled by ATP-Induced Cytoskeletal Defects. *Biophys. J.* **2005**, *88* (3), 1859–1874. https://doi.org/10.1529/biophysj.104.045328.
(35) Girard, P.; Prost, J.; Bassereau, P. Passive or Active Fluctuations in Membranes Containing Proteins. *Phys. Rev. Lett.* **2005**, *94* (8), 088102. https://doi.org/10.1103/PhysRevLett.94.088102.